Effect of Molybdenum on the Activity Temperature Enlarging of Mn-Based Catalyst for Mercury Oxidation

Bo Zhao [1,2], Xiaojiong Zhao [2], Yangshuo Liang [1], Yu Wang [1], Linbo Qin [1,*] and Wangsheng Chen [1]

[1] Hubei Key Laboratory for Efficient Utilization and Agglomeration of Metallurgic Mineral Resources, Wuhan 430081, China; zhaobo87@wust.edu.cn (B.Z.); liangyangshuo@126.com (Y.L.); yuwang@wust.edu.cn (Y.W.); chenwangsheng@wust.edu.cn (W.C.)

[2] Industrial Safety Engineering Technology Research Center of Hubei Province, Wuhan University of Science and Technology, Wuhan 430081, China; jiongwust@163.com

* Correspondence: qinlinbo@wust.edu.cn

Abstract: The MnO_2/TiO_2 (TM_5) catalyst modified by molybdenum was used for mercury oxidation at different temperatures in a fixed-bed reactor. The addition of molybdenum into TM_5 was identified as significantly enlarging the optimal temperature range for mercury oxidation. The optimal mercury oxidation temperature of TM_5 was only 200 °C, with an oxidation efficiency of 95%. However, the mercury oxidation efficiency of TM_5 was lower than 60% at other temperatures. As for MnO_2–MoO_3/TiO_2 (TM_5Mo_5), the mercury oxidation efficiency was above 80% at 200–350 °C. In particular at 250 °C, the mercury oxidation efficiency of TM_5Mo_5 was over 93%. Otherwise, the gaseous O_2, which could supplement the lattice oxygen in the catalytic reaction, played an important role in the process of mercury oxidation over TM_5Mo_5. The results of X-ray photoelectron spectroscopy (XPS) suggested that mercury oxidized by O_2 over TM_5Mo_5 followed the Mars–Maessen mechanism.

Keywords: mercury oxidation; MnO_2–MoO_3/TiO_2; temperature; mars–maessen mechanism

1. Introduction

Coal-fired power plants are among the largest mercury emission sources from anthropogenic activities [1]. Because of its toxicity to the environment and human health, mercury emission from coal-fired power plants has been strictly limited in the United States [2]. In China, a mercury emission limitation of 0.03 mg/m^3 was announced in the Emission Standard of Air Pollutants for Thermal Power Plants (GB13223-2011). Additionally, the Chinese government deposited the ratification of the Minamata Convention on Mercury, and became the 30th country of the Convention on August 31st, 2016. This means that the limit of mercury emission from coal-fired power plants in China will be stricter [3].

Mercury exists as three forms in coal combustion flue gas: elemental mercury (Hg^0), oxidized mercury (Hg^{2+}), and particle-bound mercury (Hg^p) [4]. Hg^{2+} and Hg^p can be easily eliminated by wet flue gas desulphurization (WFGD) and electrostatic precipitator (ESP) [5], respectively. However, Hg^0 is difficult to capture by existing air pollution control devices due to its water insolubility and volatility. In the past 20 years, the methods of mercury removal, such as adsorption by sorbents [6,7] and oxidization by oxidants [8] or catalysts [9,10], have been widely investigated. Catalytic oxidation of Hg^0 was in the spotlight when the selective catalytic reduction (SCR) system in coal-fired power plants was found to be beneficial for elemental mercury oxidation [11,12]. Hence, a variety of catalysts for mercury oxidation have been developed recently. Metal oxides, such as V_2O_5 [13,14], Fe_2O_3 [15], CeO_2 [16], MnO_2 [17], CuO [18], etc., have been loaded as active ingredients on the catalysts for mercury

oxidation. Peña et al. [19] found that the catalytic activity of the catalysts followed the sequence Mn > Cu > Cr > Co > Fe > V > Ni, which indicated that an Mn-based catalyst was an excellent choice for mercury oxidation. Ji et al. [20] reported that MnO_2/TiO_2 was available for Hg^0 oxidation and NO reduction simultaneously at 200 °C, with a mercury oxidation efficiency of 90% and NO conversion efficiency of 97%. Wu et al. [21] indicated that Mn-based catalysts were beneficial for mercury oxidation, and elemental mercury removal efficiency follows the order 4% Mn/MK10 (montmorillonite K 10) > 4% Mn/SiO_2 > 4% Mn/TiO_2 > 4% Mn/Al_2O_3. In particular for the Mn/montmorillonite K 10, the mercury removal efficiency was greater than 90% [22]. However, mercury oxidation ability of MnO_2/TiO_2 was significantly restrained in the presence of SO_2, and more than 80% of Hg^0 escaped [20]. The optimal temperature of the Mn-based catalyst for mercury oxidation was always lower than 250 °C, and the formation of NH_4HSO_4 was the main reason for the catalyst deactivation at low temperature [23]. One way to enhance mercury oxidation ability was to add various auxiliary metal components into the Mn-based catalyst and keep low-temperature activity. Ce [17,24,25], Fe [3,15], and Co [16] were extensively loaded into the Mn-based catalyst. Li et al. [19] reported that the Mn–Ce/Ti catalyst exhibited high mercury oxidation ability at 150–250 °C. He et al. [25] stated that 6% Ce–6% MnO_x/Ti–PILC exhibited optimal mercury oxidation ability at 250 °C, with a mercury oxidation efficiency of 72%.

Another way to avoid NH_4HSO_4 being deposited on the catalyst was to enhance the activity temperature of the Mn-based catalyst for mercury oxidation. In general, less NH_4HSO_4 was formed on the catalyst after the temperature rose above 300 °C, so enhancing the activity temperature of Mn-based catalyst to above 300 °C might be valuable. Existing research proves that molybdenum is a beneficial auxiliary component in V_2O_5/TiO_2. Mercury oxidation efficiency of V_2O_5–MoO_3/TiO_2 was higher than that of V_2O_5/TiO_2. More importantly, the active temperature range was enlarged to 350°C [26]. SCR activity of $V_2O_5/MO_3/TiO_2$ was higher than that of $V_2O_5/WO_3/TiO_2$ at 300 °C [27]. Fewer sulfates were considered to deposit on V/Mo/Ti–S catalyst [28]. Furthermore. More acid sites were also discovered after the addition of Mo into Ce/Ti catalyst, which contributed to the enhancement of SCR activity [29]. Therefore, to increase the active temperature of MnO_2/TiO_2 for mercury oxidation, the addition of molybdenum to this catalyst may be feasible. Moreover, few studies have focused on the mercury oxidation over Mn–Mo/Ti catalyst, and no research about the role of molybdenum in the catalyst for mercury oxidation has been reported. To develop a more widely applicable Mn-based catalyst, it is worth investigating whether the addition of molybdenum to MnO_2/TiO_2 enlarge the active temperature range of this Mn-based catalyst.

To clarify this question, in this study, Mn–Mo/Ti catalyst was prepared and the performance of this catalyst on mercury oxidation in simple O_2/N_2 atmosphere at different temperature was investigated. In addition, the mechanism of mercury oxidized by O_2 over Mn–Mo/Ti was also examined.

## 2. Results and Discussion

2.1. Catalyst Characterization

2.1.1. Brunauer–Emmett–Teller (BET)

The pore structure parameters of the three catalysts are listed in Table 1. BJH is the abbreviation of "Barrett Joyner Halenda", meaning the pore size distribution, which refers to the percentage of pore size at all levels in the material calculated by quantity or volume. The Brunauer–Emmett–Teller (BET) surface area of TM_5 was 81 m^2/g, and this value decreased to 56 m^2/g after the addition of 5 wt. % MoO_3 into the catalyst. Moreover, the BET surface area of TMo_5 was only 26 m^2/g. Figure 1 was the pore diameter distribution of the three catalysts. The pore volume of TM_5Mo_5 (0.0507 cm^3/g) was lower than that of both TM_5 (0.0936 cm^3/g) and TMo_5 (0.0639 cm^3/g). The addition of molybdenum to TM_5 caused both the surface area and pore volume to decrease, which indicated that the interaction might be held between these compositions.

Table 1. The BET surface area of the three catalysts.

Catalysts	BET Surface Area/m²/g	BJH Pore Volume/cm³/g	BJH Average Diameter/nm
TM_5	80.8678	0.0936	4.5871
TM_5Mo_5	55.7141	0.0507	3.8020
TMo_5	25.9037	0.0639	9.3176
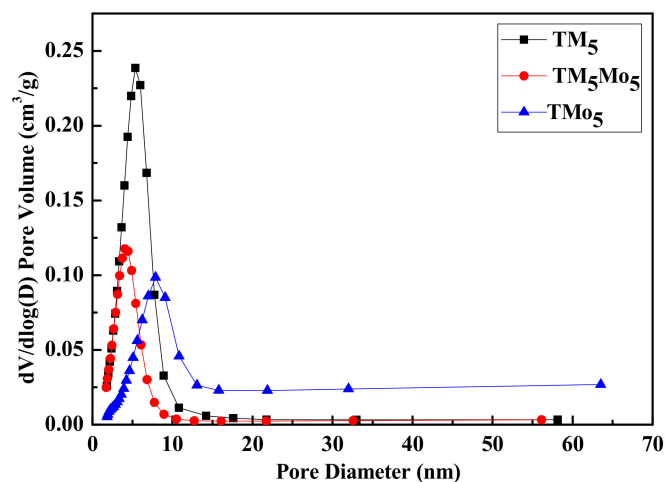
Figure 1. The pore diameter distribution of the catalysts.

2.1.2. Scanning Electron Microscopy (SEM)

Figure 2 shows the scanning electron microscopy (SEM) images of TM_5 and TM_5Mo_5. It is clearly revealed that the addition of molybdenum can significantly change the morphology of the catalyst. Comparing these two catalysts, the surface morphology of TM_5Mo_5 was much smoother than that of TM_5, and roughly melted materials were exhibited on the surface of TM_5Mo_5. This is mainly because molybdenum tends to aggregate during the process of catalyst preparation, where molybdenum was added to calcine titanic acid [30]. Few pores existed at the surface of both catalysts, which was consistent with the results of BET analysis.
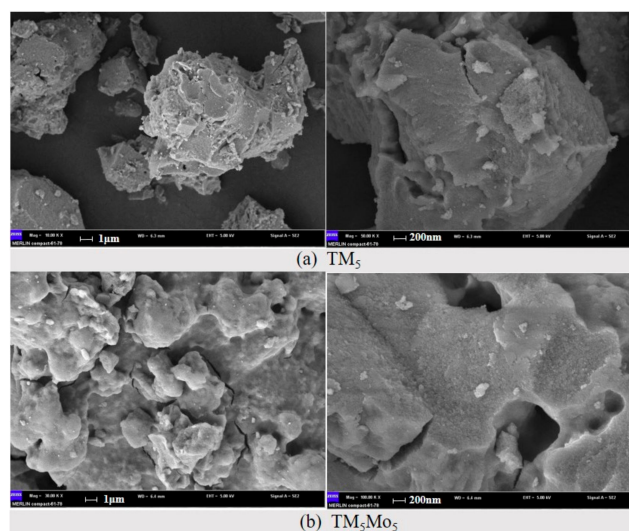
Figure 2. The scanning electron microscopy (SEM) images of (**a**) TM_5 and (**b**) TM_5Mo_5.

2.1.3. X-ray Powder Diffraction (XRD)

Figure 3 displays the X-ray powder diffraction (XRD) patterns of the three catalysts. Only two types of crystalline were identified in both TM_5Mo_5 and TM_5, which were the anatase and rutile of

TiO_2. The crystalline at 25.2° was the typical peak of anatase [26], which was in all three catalysts. No crystal phase of MoO_3 and MnO_2 was discovered on the surface of TM_5Mo_5 and TM_5. However, a crystalline at 32° was found in TMo_5, which was the peak of MoO_3 according to the result of the joint committee on power diffraction standards (JCPDS). This indicates that the crystal phase of MoO_3 tends to change into a non-crystalline state after Mn and Mo are both present in the catalysts. This may be caused by the interaction of Mn and Mo during the process of catalyst preparation [30]. As for TM_5Mo_5 and TM_5, both molybdenum and manganese oxides were present in either as small crystallites (less than 4 nm in diameter) or non-crystalline state [27].
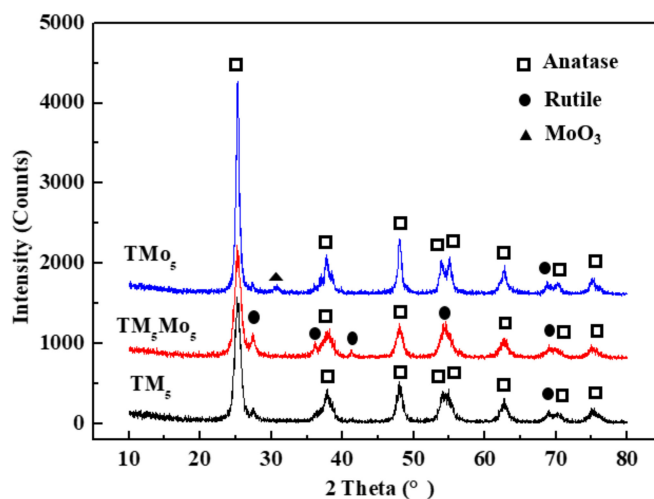

Figure 3. The X-ray powder diffraction (XRD) results of the three catalyst.

2.1.4. X-ray Photoelectron Spectroscopy (XPS)

Mn 2p results of TM_5 and TM_5Mo_5 are shown in Figure 4. Two peaks of Mn 2p 3/2 are exhibited at 636–647 eV, which are respectively Mn^{2+} at 641 eV and Mn^{4+} at 642.4 eV on the surface of TM_5 in Figure 4a [8,31]. Two peaks of Mn 2p 3/2 are also noted at 636–647 eV on the surface of TM_5Mo_5 after the addition of MoO_3, which are Mn^{3+} at 641.7 eV and Mn^{4+} at 642.8 eV [8]. Comparing the results in Figure 4a,b, higher valence manganese was discovered on the surface of TM_5Mo_5. It should be noted that the addition of molybdenum enhanced the binding energy of manganese oxide transformed to high electron bit. Research into typical SCR catalysts (V–Mo/Ti) clarified that the presence of both molybdenum and vanadium in the catalyst cause the formation of stronger acid sites because of the interaction of Mo and V on surface of the catalysts [27], and molybdenum oxide could assist in oxidization of vanadium in low valence to higher valence [26]. As for TM_5Mo_5, the same effect of molybdenum might cause the change of electron bit of manganese in TM_5 and TM_5Mo_5, since the interaction of Mn and Mo during the process of catalysts preparation may occur depending on the results of XRD analysis.
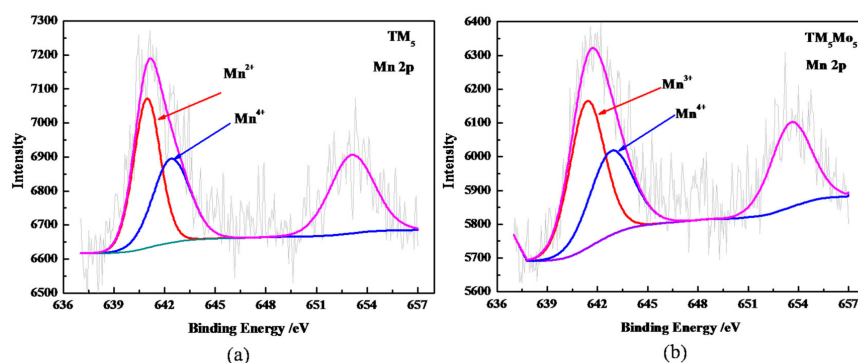
Figure 4. The XPS analysis of Mn 2p for (**a**) TM_5; and (**b**) TM_5Mo_5.

Figure 5 shows the O 1 s results of the three catalysts. Four peaks of O 1 s are discovered at 526–534 eV on the surface of TM_5, which are TiO_2 at 529 eV and 530.1 eV, Ti_2O_3 at 531.1 eV, MnO_x at 529.5 eV, respectively. In Figure 5b, three peaks, which are TiO_2 at 529.7 eV, MoO_3 at 530.4 eV and Ti_2O_3 at 531.1 eV, were consulted on the surface of TMo_5. Four peaks, which are TiO_2 at 530 eV and 529.3 eV, MoO_3 at 530.48 eV and $TiO_{0.73}$ at 531.5 eV, are found on the surface of TM_5Mo_5. The addition of MnO_2 significantly weakened the intensity of TiO_2, which means that the surface of TM_5Mo_5 became complex for the interaction between manganese and molybdenum. In Figure 5c, the Mn–O component disappeared, but this does not mean that there were no Mn–O components on the surface of TM_5Mo_5. During the X-ray photoelectron spectroscopy (XPS) analysis of O 1 s, the binding energy of peaks for TiO_2 and MnO_x was partly overlapped, e.g., the peak of 529.3 eV was TiO_2 and the peak at 529.5 eV was MnO_x, and TiO_2 accounts for most of the catalyst. Mn–O components on the surface of TM_5Mo_5 were hidden, especially after the addition of Mo, because of the binding energy of peaks for TiO_2 was transferred to near 529.5 eV. Therefore, XPS analysis of Mn 2p in Figure 6 was the main basis for the following results.
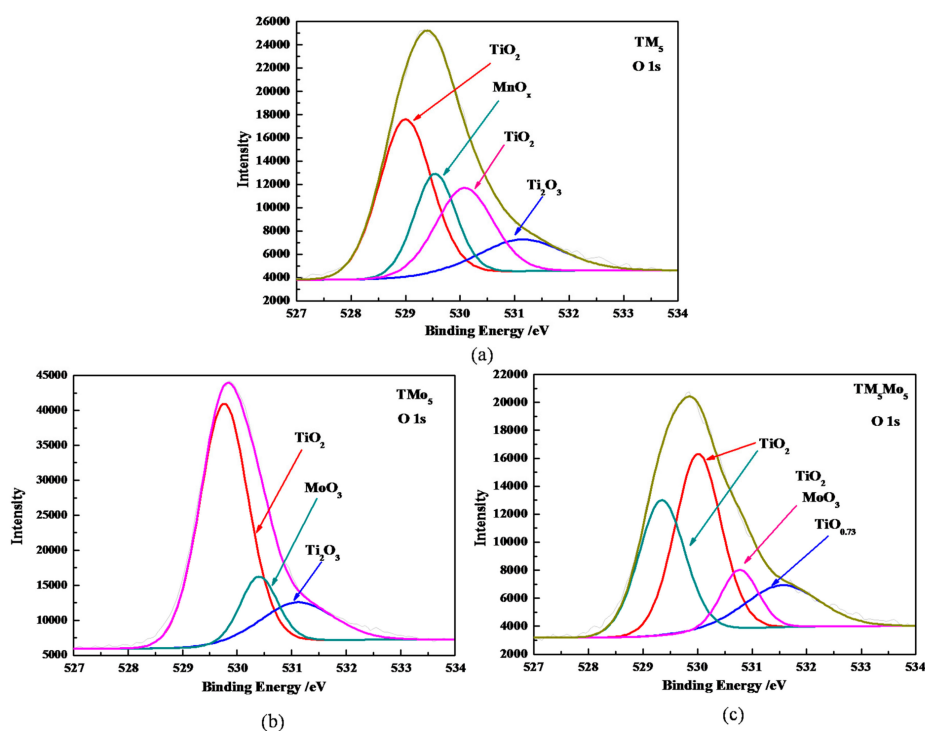

Figure 5. The XPS analysis of O 1 s for (**a**) TM_5; (**b**) TMo_5 and (**c**) TM_5Mo_5.
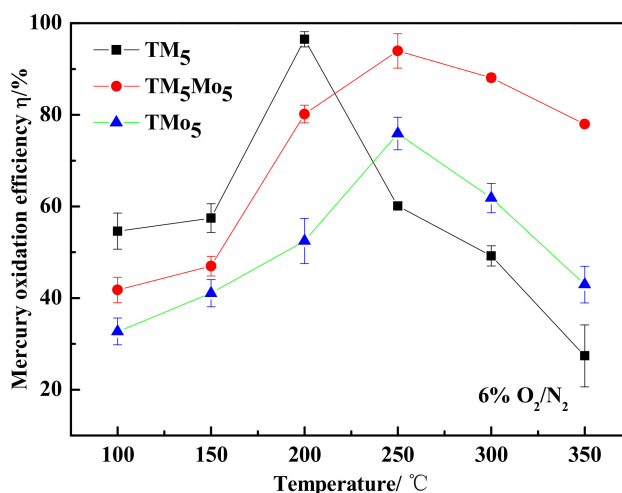
Figure 6. The effect of temperature on mercury oxidation over TM_5Mo_5.

2.2. Effect of Temperature

Figure 6 exhibits the effect of temperature on mercury oxidation over these catalysts in 6% O_2/N_2. The mercury oxidation efficiency of TM_5 increased as the temperature rose from 100 °C to 200 °C. However, this value of TM_5 decreased immediately when the temperature was above 200 °C. The optimal temperature range of TM_5 for mercury oxidation was only at the point of 200 °C, with mercury oxidation efficiency over 95%. Mercury oxidation efficiency of TM_5 decreased to 60% at 250 °C, 49% at 300 °C, and 27% at 350 °C, respectively. As for TM_5Mo_5, the mercury oxidation efficiency rose as the temperature increased. Mercury oxidation efficiency of TM_5Mo_5 was over 80% when the temperature was above 200 °C, and the optimal mercury oxidation efficiency was 93% at 250 °C. Moreover, this value was 88% at 300 °C and 77% at 350 °C, respectively. As for TMo_5, the best mercury oxidation efficiency was only 76% at 250 °C. Ji et al. [20] reported that the optimal mercury oxidation efficiency of MnO_2/TiO_2 was 90%, and Wu et al. [21] also proved that the best mercury oxidation efficiency of Mn-based catalyst was over 90%. Reporting on the above research, the Mn-based catalyst in this work also had similar mercury oxidation ability.

The results in Figure 6 indicate that the addition of molybdenum to TM_5 not only enhances the mercury oxidation ability, but also expands the optimal temperature range of mercury oxidation over TM_5Mo_5. Marshneva et al. [13] points out that molybdenum could improve the activity of the SCR catalyst in the De–NO$_x$ process. The sulfur resistance of molybdenum was discovered in the Mn/α-Al$_2$O$_3$ catalyst for mercury oxidation [32]. The primary result was that the addition of molybdenum could optimize the structure of the catalyst and promote the main active site transformation to a more active state. Additionally, other curious phenomena were also displayed in Figure 6. When the temperature was below 200 °C, the mercury oxidation ability of the three catalysts followed in the order TM_5 > TM_5Mo_5 > TMo_5. However, the order was changed to TM_5Mo_5 > TMo_5 > TM_5, when the temperature was over 250 °C. Existing research states that mercury oxidation over catalyst follows two primary steps: Hg^0 should be first adsorbed on the catalyst surface, and then the adsorbed mercury is oxidized by the oxidizing components on the catalyst surface. The BET surface area of the three catalysts follows the order TM_5 > TM_5Mo_5 > TMo_5, and this was consistent with the mercury oxidation ability of the three catalysts at temperatures below 200 °C. This implies that the first step determines the mercury oxidation efficiency of the catalysts when the temperature is below 200 °C. During this temperature range, Hg^0 is more easily physically adsorbed on the surface of TM_5 due to having the highest surface area of the three catalysts. When the temperature is above 250 °C, the advantage of the BET surface area is weakened. Instead, oxidizing components on the catalyst surface play a primary role in the process of mercury oxidation over these catalysts. The XPS analysis results suggest that a much higher quantity of manganese is in the high-valance state on the surface of TM_5Mo_5, which is the core component for

mercury oxidation. Therefore, mercury oxidation efficiency of TM_5Mo_5 is higher than that of other two catalysts at temperatures above 250 °C.

2.3. Effect of O_2

Figure 7 shows the mercury oxidation efficiency of TM_5Mo_5 in two conditions, with or without 6% O_2 at 250 °C. It shows that the mercury oxidation efficiency of TM_5Mo_5 in 6% O_2/N_2 is 93% and the value is only 45% in pure N_2 after 2 h. It suggests that O_2 plays an important role in the process of Hg^0 oxidation over TM_5Mo_5. It has been shown that Hg^0 oxidized by O_2 over catalyst mainly follows the Mars–Maessen mechanism [5,8,26]. Equations (1)–(4) describe the reaction process. Besides the primary two steps mentioned in Section 3.2, the third step highlights the effect of oxygen in the circle of the catalytic reaction. As for TM_5Mo_5, elemental mercury is first adsorbed on the catalyst surface; subsequently, the adsorbed elemental mercury is oxidized by manganese in high valance, such as MnO_2 and Mn_2O_3. The manganese in high valance itself is reduced to the lower valance, which mainly is MnO. In pure N_2 condition, no oxidizing substance is supplied in the atmosphere; after MnO_2 or Mn_2O_3 is reduced to MnO, the reduced manganese cannot be re-oxidized to a high-valance state. Therefore, mercury oxidation efficiency of TM_5Mo_5 decreases and the value is lower than 45% after 2 h. In 6% O_2/N_2, as the oxidability of O_2, MnO could be re-oxidized to MnO_2 or Mn_2O_3. Accordingly, more elemental mercury could be oxidized by the oxidizing substance on the surface of TM_5Mo_5 and the value was even higher than 93% after 2 h tests.
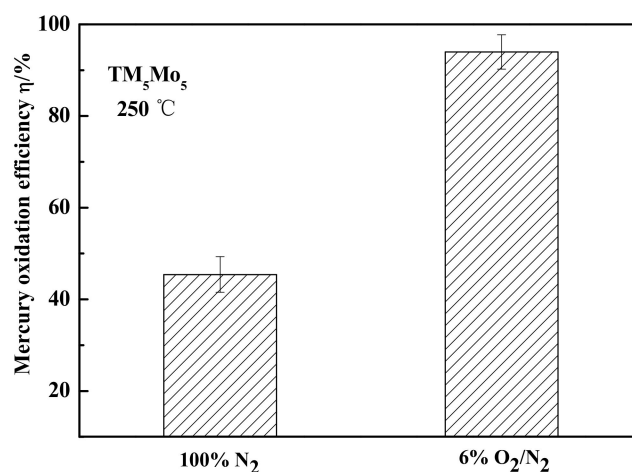
$$A(g) \leftrightarrow A(ads) \tag{1}$$

$$A(ads) + M_xO_y \rightarrow AO(ads) + M_xO_{y-1} \tag{2}$$

$$M_xO_{y-1} + 1/2O_2 \rightarrow M_xO_y \tag{3}$$

$$AO(ads) \rightarrow AO(g) \tag{4}$$

Figure 7. The effect of oxygen on mercury oxidation over TM_5Mo_5.

2.4. Stability Test

To clarify the mechanism of mercury oxidation over TM_5Mo_5, a type of 20 h tests in 6% O_2/N_2 atmosphere at 200 °C and 300 °C was designed. It represents the low-temperature mercury oxidation ability of TM_5Mo_5 at 200 °C, while it represents the high-temperature mercury oxidation ability of TM_5Mo_5 at 300 °C. Figure 8 shows that mercury oxidation efficiency of TM_5Mo_5 was in the range of 88% to 93% at 300 °C, while the value was 78% to 83% at 200 °C during the 20 h tests. This indicates that the mercury oxidation ability of TM_5Mo_5 is much stronger at 300 °C than at 200 °C. In addition, mercury oxidation efficiency of TM_5Mo_5 is steady at both temperatures. To explain this phenomenon,

XPS was introduced to characterize the tested samples. Figure 9 shows the Mn 2p results of the two tested samples. MnO, Mn_2O_3, and MnO_2 were discovered on the surface of both samples. The result of Figure 4b shows that no MnO exists on the surface of initial TM_5Mo_5. This illustrates that elemental mercury is mainly oxidized by Mn_2O_3 and MnO_2 on the surface of TM_5Mo_5, and partial MnO is formed on the catalyst surface[41]. Additionally, peak area ratio of Mn_2O_3 and MnO_2 in Figure 9a was 0.31, and the ratio increased to 0.79 in Figure 9b. This was in accordance with the results of the mercury oxidation ability at these two temperatures. When the catalytic reaction was steady, more Mn^{4+} on the surface participated in the reaction at 300 °C than that at 200 °C. Therefore, the quantity of MnO_2 at 300 °C was less than that at 200 °C and the mercury oxidation ability was to the contrary. This proves that the main active component for mercury oxidation is manganese in high valance and the addition of molybdenum enhanced the mercury oxidation ability of MnO_2–MoO_3/TiO_2.
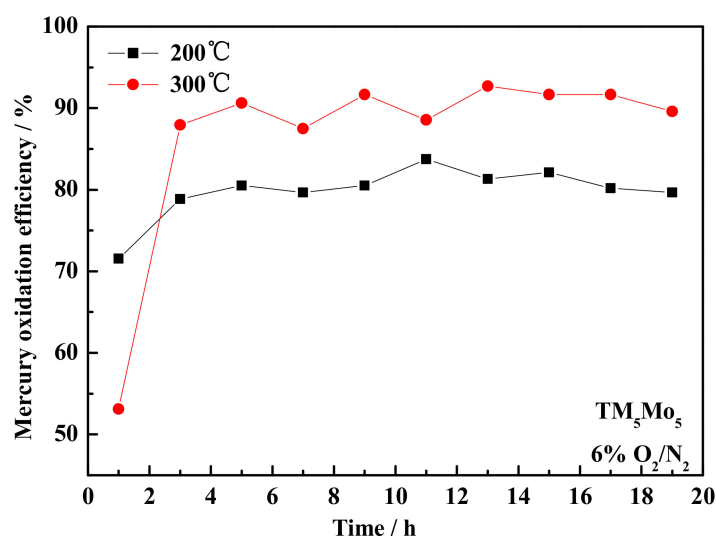

Figure 8. Long time test of the mercury oxidation over TM_5Mo_5 at 200 and 300 °C.
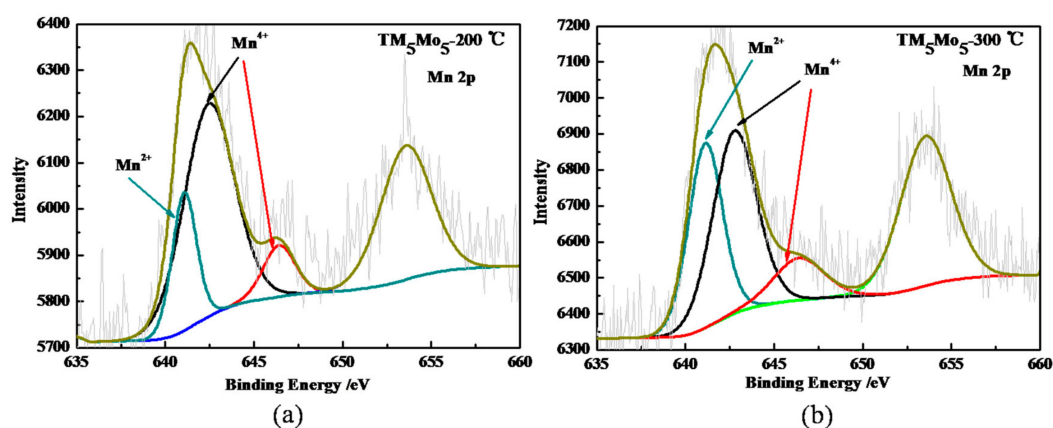

Figure 9. XPS results of long-term test samples: (**a**) 20 h test at 200 °C; (**b**) 20 h test at 300°.

3. Experimental

3.1. Catalyst Preparation

The catalysts were prepared by sol–gel method, and a detailed synthesis process is shown in Figure 10. Main raw materials were tetrabutyl titanate, ethanol, ammonia, nitric acid, molybdenum trioxide, and $Mn(NO_3)_2$ solution. All the chemical reagents were analytically pure. The tetrabutyl titanate was first dissolved in isometric volume ethanol solution to develop the sol. Then ammonia, nitric acid, manganese nitrate, and molybdenum were successively included in the solution. After

blending, drying, calcining, and grinding, the catalysts were pulverized to 45–100 μm. Three kinds of catalysts, named TM_5 (5 wt. % MnO_2), TM_5Mo_5 (5 wt. % MnO_2 and MoO_3) and TMo_5 (5 wt. % MoO_3) were prepared in this study.
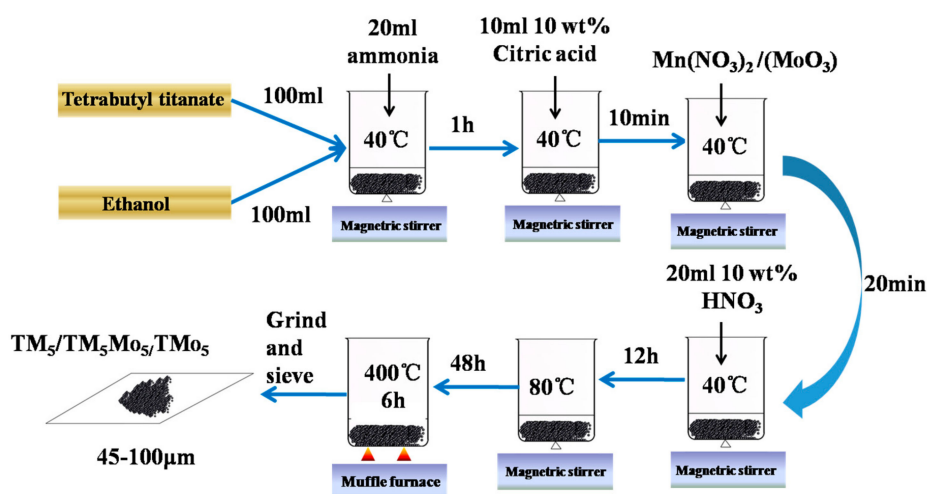

Figure 10. The progress of catalysts preparation.

3.2. Characterization Equipment

The Brunauer–Emmett–Teller (BET) surface area and pore size distribution were controlled by ASAP 2020 (Micromeritics, America) [33–35]. X-ray photoelectron spectroscopy (XPS) and XRD of the three catalysts were determined by VG Multilab 2000 X-ray Photoelectron Spectroscopy and X'pert PRO X-ray powder diffraction (PANalytical, Holland) [36–38], respectively. Sirion 200 scanning electron microscope (FEI, Holland) was used to characterize the SEM of the three catalysts [39].

3.3. Experimental Conditions

Mercury oxidation ability of the three catalysts was tested on a laboratory scale fixed-bed experimental system. As showed in Figure 11, the experimental system was made up of three parts: a fixed-bed reactor, a mercury permeation source, and a mercury detection device. Detailed information of the fixed-bed reactor and mercury permeation source has been described in other research [26]. The fixed-bed reactor was a vertical furnace, and a quartz tube (ID: 16 mm) with a length 550 mm was equipped in the furnace. A sieve plate used to load the catalyst was in the middle of the quartz tube. The mercury permeation source was a U-shaped quartz tube, which was placed in a thermostat-controlled water bath. The mercury permeation tube was positioned in the U-shaped quartz tube, and mercury was transported out by N_2. The elemental mercury concentration was determined by QM201G (measuring ranges: 0–100 μg/L, Sensitivity: 0.1 μg/L, Qing'an Inc. Changzhou, China). Before each test, the mercury content standard curve of QM201G was determined. The initial Hg^0 concentration in the experimental flue gas was 55 ± 2 μg/m^3. The total flow rate of each experiment was 1 L/min, and elemental mercury was transported by 0.5 L/min N_2. The weight of the catalyst in each run was 0.15 g, and the gas reciprocal space velocity was over 180,000 h^{-1}, which was calculated by dividing the volume of the catalyst by the volume of gas passing through the reactor in one hour. The experimental conditions are listed in Table 2.
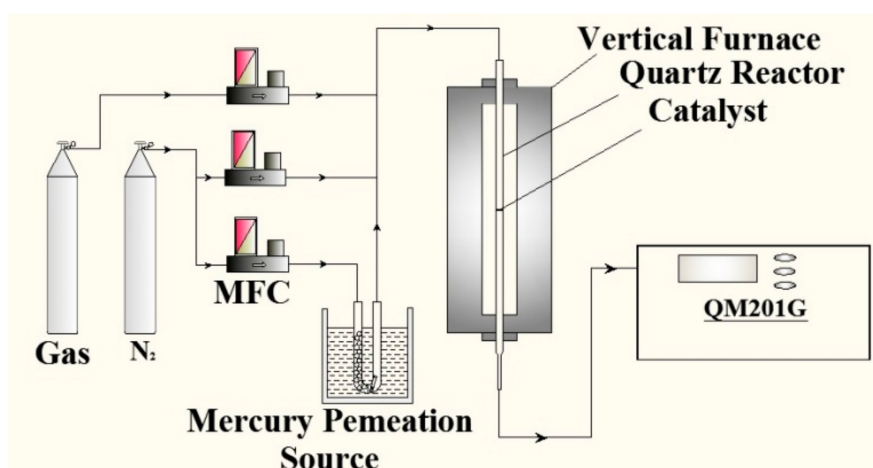
Figure 11. The experimental system.

Table 2. The experimental conditions.

Experiments	Catalysts	Experimental Conditions
Impact of temperature	TM5Mo5/TM5/TMo5	6% O_2/N_2, 100 °C/150 °C/200 °C/250 °C/00 °C/350 °C
Impact of oxygen	TM5Mo5	100% N_2/6% O_2/N_2, 250 °C

Mercury oxidation efficiency was used to describe Hg^0 oxidized ability of the catalysts. This was determined by Equation (5), and a detailed introduction of this equation has been made in other research [10,17,26,40]. When the mercury content at the outlet of the reactor was varied below the range of 5% in 1 h, it could be assumed that the experiment reached a stable state. To ensure the accuracy of the results, every experiment was replicated three times.

$$\eta = \frac{\Delta Hg^0}{Hg^0_{in}} = \frac{\Delta Hg^0 - Hg^0_{out}}{Hg^0_{in}} \times 100\% \tag{5}$$

η: The mercury oxidation efficiency of the catalyst
Hg^0_{in}: The elemental mercury concentration at the inlet of the reactor
Hg^0_{out}: The elemental mercury concentration at the outlet of the reactor

4. Conclusions

This work focused on the unique performance of mercury oxidation over MnO_2–(MoO_3)/TiO_2. XPS was put in place to clarify the mechanism of mercury oxidation over this catalyst. Molybdenum enhanced manganese transference from a low-valance state to a high-valance state, which increased the active sites on the surface of the catalyst for mercury oxidation. Molybdenum effectively widened the optimal temperature range of the catalyst for mercury oxidation. The optimal temperature of TM5 for mercury oxidation was only a point at 200 °C, while the best temperature range of TM5Mo5 for mercury oxidation was 200 to 350 °C. O_2 plays an important role for mercury oxidation over TM5Mo5, and this process follows the Mars–Maessen mechanism. Long-term tests indicated that the oxygen component of the catalyst surface was more active at 200 °C than that at 300 °C.

Author Contributions: Writing—review & editing, B.Z.; Data curation, X.Z.; Writing—original draft, Y.L.; Methodology, Y.W.; Resources, L.Q. & W.C. All authors have read and agreed to the published version of the manuscript.

References

1. Huggins, F.E.; Senior, C.L.; Chu, P.; Ladwig, K.; Huffman, G.P. Selenium and arsenic speciation in fly ash from full-scale coal-burning utility plants. *Environ. Sci. Technol.* **2007**, *41*, 3284–3289. [CrossRef] [PubMed]

2. Han, J.; Xiong, Z.; Zhao, B.; Liang, Y.; Wang, Y.; Qin, L. A prediction of arsenic and selenium emission during the process of bituminous and lignite coal co-combustion. *Chem. Pap.* **2020**. [CrossRef]

3. Yang, J.; Zhao, Y.; Liang, S.; Zhang, S.; Ma, S.; Li, H.; Zhang, J.; Zheng, C. Magnetic iron–manganese binary oxide supported on carbon nanofiber ($Fe_{3−x}Mn_xO_4$/CNF) for efficient removal of Hg0 from coal combustion flue gas. *Chem. Eng. J.* **2018**, *334*, 216–224. [CrossRef]

4. Galbreath, K.C.; Zygarlicke, C.J. Mercury speciation in coal combustion and gasification flue gases. *Environ. Sci. Technol.* **1996**, *30*, 2421–2426. [CrossRef]

5. Presto, A.A.; Granite, E.J. Survey of catalysts for oxidation of mercury in flue gas. *Environ. Sci. Technol.* **2006**, *40*, 5601–5609. [CrossRef]

6. Cao, T.; Li, Z.; Xiong, Y.; Yang, Y.; Xu, S.; Bisson, T.; Gupta, R.; Xu, Z. Silica-silver nanocomposites as regenerable sorbents for hg0 removal from flue gases. *Environ. Sci. Technol.* **2017**, *51*, 11909–11917. [CrossRef]

7. Lopez-Anton, M.A.; Gil, R.R.; Fuente, E.; Díaz-Somoano, M.; Martínez-Tarazona, M.R.; Ruiz, B. Activated carbons from biocollagenic wastes of the leather industry for mercury capture in oxy-combustion. *Fuel* **2015**, *142* (Suppl. C), 227–234. [CrossRef]

8. Zhou, Z.; Liu, X.; Hu, Y.; Xu, J.; Cao, X.E.; Liao, Z.; Xu, M. Investigation on synergistic oxidation behavior of NO and Hg^0 during the newly designed fast SCR process. *Fuel* **2018**, *225*, 134–139. [CrossRef]

9. Cheng, J.; Wang, X.; Li, Y.; Ning, P. Adsorption and catalytic oxidation of mercury over MnO_x/TiO_2 under low-temperature conditions. *Ind. Eng. Chem. Res.* **2017**, *56*, 14419–14429. [CrossRef]

10. Wang, P.; Su, S.; Xiang, J.; You, H.; Cao, F.; Sun, L.; Hu, S.; Zhang, Y. Catalytic oxidation of Hg0 by MnO_x–CeO_2/γ-Al_2O_3 catalyst at low temperatures. *Chemosphere* **2014**, *101* (Suppl. C), 49–54. [CrossRef]

11. Eswaran, S.; Stenger, H.G. Understanding mercury conversion in selective catalytic reduction (SCR) catalysts. *Energy Fuels* **2005**, *19*, 2328–2334. [CrossRef]

12. Machalek, T.; Ramavajjala, M.; Richardson, M.; Richardson, C.; Dene, C.; Goeckner, B.; Anderson, H.; Morris, E. Pilot Evaluation of Flue Gas Mercury Reactions Across an SCR Unit. In Proceedings of the Environmental Protection Agencys Air and Waste Management Association Combined Power Plant Air Pollution Control Symposium, Washington, DC, USA, 19–22 May 2003. Paper No. 64.

13. Marshneva, V.I.; Slavinskaya, E.M.; Kalinkina, O.V.; Odegova, G.V.; Moroz, E.M.; Lavrova, G.V.; Salanov, A.N. The influence of support on the activity of monolayer vanadia-titania catalysts for selective catalytic reduction of NO with ammonia. *J. Catal.* **1995**, *155*, 171–183. [CrossRef]

14. Zhao, B.; Han, J.; Qin, L.; Chen, W.; Zhou, Z.; Xing, F. Impact of individual flue gas components on mercury oxidation over a V_2O_5–MoO_3/TiO_2 catalyst. *New J. Chem.* **2018**, *42*, 20190–20196. [CrossRef]

15. Xiong, S.; Xiao, X.; Huang, N.; Dang, H.; Liao, Y.; Zou, S.; Yang, S. Elemental mercury oxidation over Fe–Ti–Mn spinel: Performance, mechanism, and reaction kinetics. *Environ. Sci. Technol.* **2017**, *51*, 531–539. [CrossRef]

16. Li, H.; Wang, S.; Wang, X.; Tang, N.; Pan, S.; Hu, J. Comparative study of Co/TiO_2, Co–Mn/TiO_2 and Co–Mn/Ti–Ce catalysts for oxidation of elemental mercury in flue gas. *Chem. Pap.* **2017**, *71*, 1569–1578. [CrossRef]

17. Li, H.; Wu, C.-Y.; Li, Y.; Zhang, J. Superior activity of MnO_x-CeO_2/TiO_2 catalyst for catalytic oxidation of elemental mercury at low flue gas temperatures. *Appl. Catal. B Environ.* **2012**, *111–112*, 381–388. [CrossRef]

18. Zhou, Z.J.; Liu, X.; Hu, Y.; Liao, Z.; Cheng, S.; Xu, M. An efficient sorbent based on $CuCl_2$ loaded CeO_2-ZrO_2 for elemental mercury removal from chlorine-free flue gas. *Fuel* **2018**, *216*, 356–363. [CrossRef]

19. Peña, D.A.; Uphade, B.S.; Smirniotis, P.G. TiO_2-supported metal oxide catalysts for low-temperature selective catalytic reduction of NO with NH_3: I. Evaluation and characterization of first row transition metals. *J. Catal.* **2004**, *221*, 421–431. [CrossRef]

20. Ji, L.; Sreekanth, P.M.; Smirniotis, P.G.; Thiel, S.W.; Pinto, N.G. manganese oxide/titania materials for removal of NOx and elemental mercury from flue gas. *Energy Fuels* **2008**, *22*, 2299–2306. [CrossRef]

21. Wu, Y.; Xu, W.; Yang, Y.; Wang, J.; Zhu, T. Support effect of Mn-based catalysts for gaseous elemental mercury oxidation and adsorption. *Catal. Sci. Technol.* **2018**, *8*, 297–306. [CrossRef]

22. Wu, Y.; Xu, W.; Yang, Y.; Shao, M.; Zhu, T.; Tong, L. Removal of gas-phase Hg^0 by Mn/montmorillonite K10. *RSC Adv.* **2016**, *6*, 104294–104302. [CrossRef]

23. Cheng, T.; Luo, L.; Yang, L.; Fan, H.; Wu, H. Formation and emission characteristics of ammonium sulfate aerosols in flue gas downstream of selective catalytic reduction. *Energy Fuels* **2019**, *33*, 7861–7868. [CrossRef]

24. Reddy, G.K.; He, J.; Thiel, S.W.; Pinto, N.G.; Smirniotis, P.G. Sulfur-tolerant Mn-Ce-Ti sorbents for elemental mercury removal from flue gas: Mechanistic investigation by XPS. *J. Phys. Chem. C* **2015**, *119*, 8634–8644. [CrossRef]

25. He, C.; Shen, B.; Li, F. Effects of flue gas components on removal of elemental mercury over Ce–MnO_x/Ti-PILCs. *J. Hazard. Mater.* **2016**, *304*, 10–17. [CrossRef] [PubMed]

26. Zhao, B.; Liu, X.; Zhou, Z.; Shao, H.; Wang, C.; Si, J.; Xu, M. Effect of molybdenum on mercury oxidized by V_2O_5–MoO_3/TiO_2 catalysts. *Chem. Eng. J.* **2014**, *253*, 508–517. [CrossRef]

27. Lietti, L.; Nova, I.; Ramis, G.; Dall'Acqua, L.; Busca, G.; Giamello, E.; Forzatti, P.; Bregani, F. Characterization and reactivity of V_2O_5–MoO_3/TiO_2 De-NOx SCR catalysts. *J. Catal.* **1999**, *187*, 419–435. [CrossRef]

28. Xu, Y.; Wu, X.; Lin, Q.; Hu, J.; Ran, R.; Weng, D. SO_2 promoted V_2O_5-MoO_3/TiO_2 catalyst for NH_3-SCR of NO_x at low temperatures. *Appl. Catal. A Gen.* **2019**, *570*, 42–50. [CrossRef]

29. Li, L.; Tan, W.; Wei, X.; Fan, Z.; Liu, A.; Guo, K.; Ma, K.; Yu, S.; Ge, C.; Tang, C.; et al. Mo doping as an effective strategy to boost low temperature NH_3-SCR performance of CeO_2/TiO_2 catalysts. *Catal. Commun.* **2018**, *114*, 10–14. [CrossRef]

30. Kwon, D.W.; Park, K.H.; Ha, H.P.; Hong, S.C. The role of molybdenum on the enhanced performance and SO_2 resistance of V/Mo-Ti catalysts for NH_3-SCR. *Appl. Surf. Sci.* **2019**, *481*, 1167–1177. [CrossRef]

31. Zhou, Z.; Liu, X.; Liao, Z.; Shao, H.; Hu, Y.; Xu, Y.; Xu, M. A novel low temperature catalyst regenerated from deactivated SCR catalyst for Hg^0 oxidation. *Chem. Eng. J.* **2016**, *304*, 121–128. [CrossRef]

32. Li, J.; Yan, N.; Qu, Z.; Qiao, S.; Yang, S.; Guo, Y.; Liu, P.; Jia, J. Catalytic oxidation of elemental mercury over the modified catalyst Mn/α-Al_2O_3 at lower temperatures. *Environ. Sci. Technol.* **2010**, *44*, 426–431. [CrossRef] [PubMed]

33. Wu, Z.; Jiang, B.; Liu, Y.; Zhao, W.; Guan, B. Experimental study on a low-temperature SCR catalyst based on MnO_x/TiO_2 prepared by sol–gel method. *J. Hazard. Mater.* **2007**, *145*, 488–494. [CrossRef] [PubMed]

34. Han, J.; Liang, Y.; Hu, J.; Qin, L.; Street, J.; Lu, Y.; Yu, F. Modeling downdraft biomass gasification process by restricting chemical reaction equilibrium with Aspen Plus. *Energy Convers. Manag.* **2017**, *153*, 641–648. [CrossRef]

35. Qin, L.; Xing, F.; Zhao, B.; Chen, W.; Han, J. Reducing polycyclic aromatic hydrocarbon and its mechanism by porous alumina bed material during medical waste incineration. *Chemosphere* **2018**, *212*, 200–208. [CrossRef]

36. Chen, W.; Hu, F.; Qin, L.; Han, J.; Zhao, B.; Tu, Y.; Yu, F. Mechanism and performance of the SCR of NO with NH_3 over sulfated sintered ore catalyst. *Catalysts* **2019**, *9*, 90. [CrossRef]

37. Huang, Z.; Qin, L.; Xu, Z.; Chen, W.; Xing, F.; Han, J. The effects of Fe_2O_3 catalyst on the conversion of organic matter and bio-fuel production during pyrolysis of sewage sludge. *J. Energy Inst.* **2019**, *92*, 835–842. [CrossRef]

38. Qin, L.; Huang, X.; Zhao, B.; Wang, Y.; Han, J. Iron oxide as a promoter for toluene catalytic oxidation over Fe–Mn/γ-Al2O3 catalysts. *Catal. Lett.* **2019**. [CrossRef]

39. Han, J.; Zhang, L.; Zhao, B.; Qin, L.; Wang, Y.; Xing, F. The N-doped activated carbon derived from sugarcane bagasse for CO_2 adsorption. *Ind. Crop. Prod.* **2019**, *128*, 290–297. [CrossRef]

40. Fan, X.; Li, C.; Zeng, G.; Gao, Z.; Chen, L.; Zhang, W.; Gao, H. Removal of gas-phase element mercury by activated carbon fiber impregnated with CeO_2. *Energy Fuels* **2010**, *24*, 4250–4254. [CrossRef]